NANO LETTERS

pubs.acs.org/NanoLett Letter

Generalized Geometric Phase for Coupled Meta-Atoms

Yue Wang,[∇] Shengjie Wu,[∇] Chen Chen,[*,∇] Xiaomin Du,[∇] Jitao Ji, Jian Li, Jiacheng Sun, Xueyun Li, Wange Song, Wei Liu,[*] Shining Zhu, and Tao Li[*]

Cite This: https://doi.org/10.1021/acs.nanolett.6c02125 Read Online

ACCESS | Metrics & More | Article Recommendations | Supporting Information

ABSTRACT: The geometric phase, such as the Pancharatnam–Berry (PB) phase, is widely employed in metasurfaces for broad functionalities. Conventional studies dominantly rely on the linear dependence of the PB phase on the orientation angle of the meta-atoms. Although some previous studies indicate the breakdown of such a linear dependence, its underlying mechanisms remain largely unknown. In this study, we provide a detailed analysis of the evolution of PB phases, unveiling the nonnegligible role of coupling among adjacent meta-atoms. From the perspective of quasi-normal modes (QNMs), we demonstrate that the PB phase is solely related to the far-field radiation polarizations of the QNMs excited, decided by both meta-atom orientations and their mutual coupling. We experimentally demonstrate these effects using a meticulously designed grating, aligning closely with our theoretical predictions. This study establishes a systematic framework for rigorous PB phase analysis, broadening the horizon for the high-precision characterization of meta-optical devices.

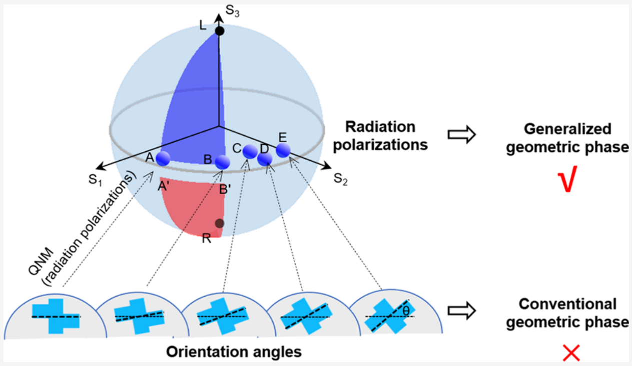

KEYWORDS: *PB phase, Metasurfaces, Quasi-normal modes, Coupling effects*

Traditional refractive lenses rely on dynamic phase (accumulated along various optical paths) for light control, inevitably leading to substantial bulkiness and constrained capabilities in tailoring the light field. In recent years, metasurface has emerged as a powerful alternative for light manipulations, making substantial breakthroughs in areas such as light deflection,[1−4] imaging,[5−9] holography,[10−15] and other fields.[16−20] Metasurfaces utilize subwavelength nanostructures to manipulate light, with their phase manipulation mechanisms roughly categorized into resonant detuning phase,[21,22] propagation dynamic phase,[23−25] and geometric phase.[26−29] Notably, the geometric phase can be easily implemented by rotating meta-atoms, making this a straightforward strategy that has been widely employed in various metasurface designs, rendering great advantages in terms of functional robustness and operational bandwidth.[30−32] For simple structures such as rectangular or elliptical atoms with a well-defined orientation angle θ, the geometric phase φ widely exploited is simply expressed as $\varphi = \pm 2\theta$,[33] which represents the *conventional geometric phase* principle with negligible coupling effects. Recent studies show that introducing more sophisticated meta-atom designs can yield additional functionalities for applications related to circular dichroism[34,35] and complex polarization control.[36] However, for these complex meta-atoms, the relationship between geometric phase and orientation angle could deviate from the conventional 2-fold linear dependence.[37−41] In such cases, traditional models are unable to capture these complex behaviors, and the design of meta-atoms has often relied on blind numerical simulations lacking clear physical insight. Thus, establishing a general theoretical framework that can systematically deepen our understanding of these complex systems is of great importance. Such a framework not only elucidates the physical origins of the geometric phase in general metasurfaces, but also provides valuable insights for the refined, high-precision analysis of a wide range of meta-optical devices with diverse functionalities.

For open optical systems, such as meta-atoms interacting with incident light, QNMs provide an alternative powerful tool for analyzing various functionalities and their underlying mechanisms. QNMs are defined as the eigenstates of nanostructures that satisfy outgoing-wave boundary conditions, and have been extensively utilized to explore the optical response of open systems.[42−48] Recently, Wang et al. reported a comprehensive QNM-based framework for the nanostructure response under arbitrary incident polarizations and directions.[49] It was revealed that the geometric phase of single meta-atom can be directly derived from the solid angle of the

Received: May 1, 2026
Revised: June 22, 2026
Accepted: June 24, 2026

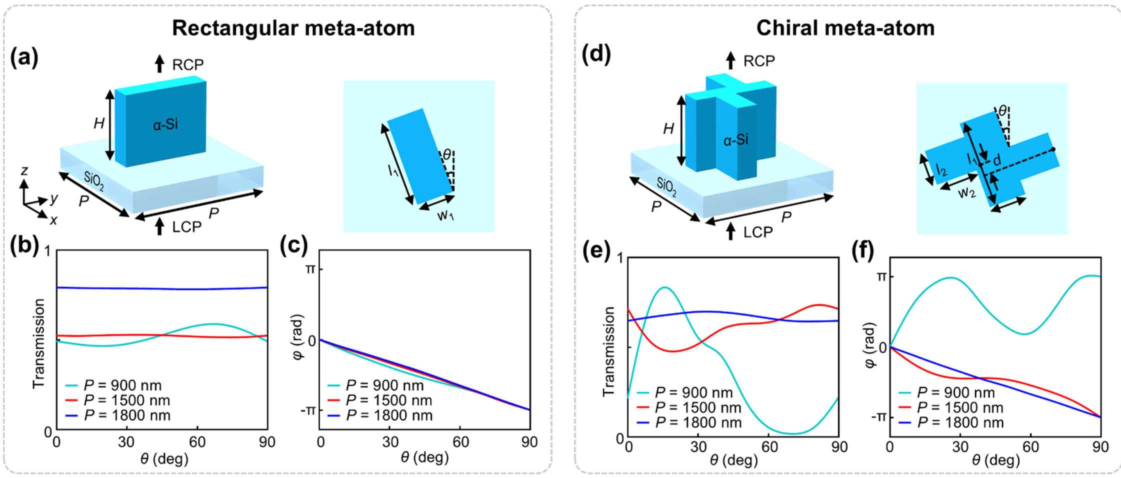

Figure 1. Schematic illustration of (a) a rectangular meta-atom and (d) a chiral structure exhibiting broken mirror symmetry. (b, e) Simulated transmission intensity and (c, f) phase shifts of the transmitted RCP component under LCP incidence at different orientation angles θ with periods of 900, 1500, and 1800 nm within a square lattice.

geodesic circuit connecting QNM far-field radiation states on the Poincaré sphere. While this work highlights the versatility of the QNMs approach for scattering problems, it does not address the complex interplay between geometric phase and orientation angle of meta-atoms in complex periodic structures that is crucial for metasurface design.

In this study, relying on the concept of QNMs and the fundamental principle of reciprocity, we established a unified framework for the rigorous interpretation of PB phase variations: it not only clarifies the origin of the conventional geometric phase in metasurfaces that exhibits a linear orientation dependence but also enables direct calculations of PB phase beyond such a conventional regime (for complex or high duty-cycle nanostructures). We demonstrate that the PB phase evolution can be attributed to the far-field polarization rotations of the QNMs of participating meta-atoms, which are correlated with both the structural orientations and mutual couplings. The PB phase response is further validated by the different beam deflection capabilities between rectangular meta-atom (with negligible coupling)-based and complex planar chiral structure (with strong coupling, referred to as chiral structure in the following for simplicity)-based metasurfaces, even though these two metasurfaces share the same distributions of meta-atom orientations. Our theory is thoroughly validated through theoretical analyses, simulations, and experimental characterizations.This work provides a clear framework for the generalized PB phase that captures the physical essence of metasurfaces with arbitrary coupling strengths, offering new physical insights into more exquisite and high-precision metasurface analysis.

At the outset, to explicitly present the coupling-induced phenomenon, we first show the optical responses of a chiral structure with broken planar mirror symmetry and, for reference, a mirror-symmetric rectangular structure under three different periods, as illustrated in Figure 1. Both the chiral and rectangular meta-atoms consist of α-Si nanopillars with a height H of 1.5 μm, arranged in a periodic square lattice with a period P on a SiO_2 substrate. The geometric parameter of the rectangular meta-atom is l_1 = 620 nm and w_1 = 250 nm. The chiral meta-atom features two extended arms from each side of the rectangular base, with l_2 = 250 nm, w_2 = 280 nm, and offset d = 85 nm. All structural parameters are labeled in Figure 1(a, d). The orientation angle of the meta-atoms is denoted as θ.

In metasurfaces, the PB phase is related to the orientation angle of the anisotropic structures and the polarization state of incident light. A widely employed scenario is circular polarization illumination with the transmission projected to circular polarization with opposite handedness. Finite-difference time-domain (FDTD) simulations are conducted to calculate the related PB phase. In these simulations, the structures are illuminated with normally incident left-circularly polarized (LCP) light along the z-direction, and the phase of the right-circularly polarized (RCP) component in the transmitted field is analyzed as a function of the structural orientation angle (see section S1 in the Supporting Information for details). The working wavelength is λ = 1550 nm, and results for P = 900, 1500, and 1800 nm are shown in Figure 1(c, f).

For the rectangular structure, the PB phase exhibits a 2-fold linear dependence on the structure orientation angle, consistent with the conventional take for granted scheme [see Figure 1(c); for smaller period (P = 900 nm), the couplings between rectangular bars also induce slight deviations from the linear dependence, but these effects are relatively weak and can therefore be neglected]. However, the PB phase of the chiral structure (an example with structural richness to provide sufficient dimensions for advanced functionalities) deviates significantly from this linear dependence at smaller periods [P = 900 and 1500 nm; see Figure 1(f)]. Here we call it a *linear-oscillated phase*, and this refers to the distorted 2-fold phase responses related to the rotation angles, i.e., $\varphi = \pm 2\theta + \delta$, where δ is the oscillated term. In addition to the PB phase, the intensities of transmitted light for both rectangular and chiral structures are also shown in Figure 1(b, e). The intensity of the transmitted light through chiral structures exhibits pronounced oscillations with respect to atom orientation (see Figure 1(e), green and red lines), in sharp contrast to the almost uniform distribution observed for the rectangular structure with different orientation angles (see Figure 1(b)). The significant difference in optical response, in both intensity and phase, between the rectangular and chiral structures can be largely attributed to the near-field coupling

https://doi.org/10.1021/acs.nanolett.6c02125
Nano Lett. XXXX, XXX, XXX−XXX

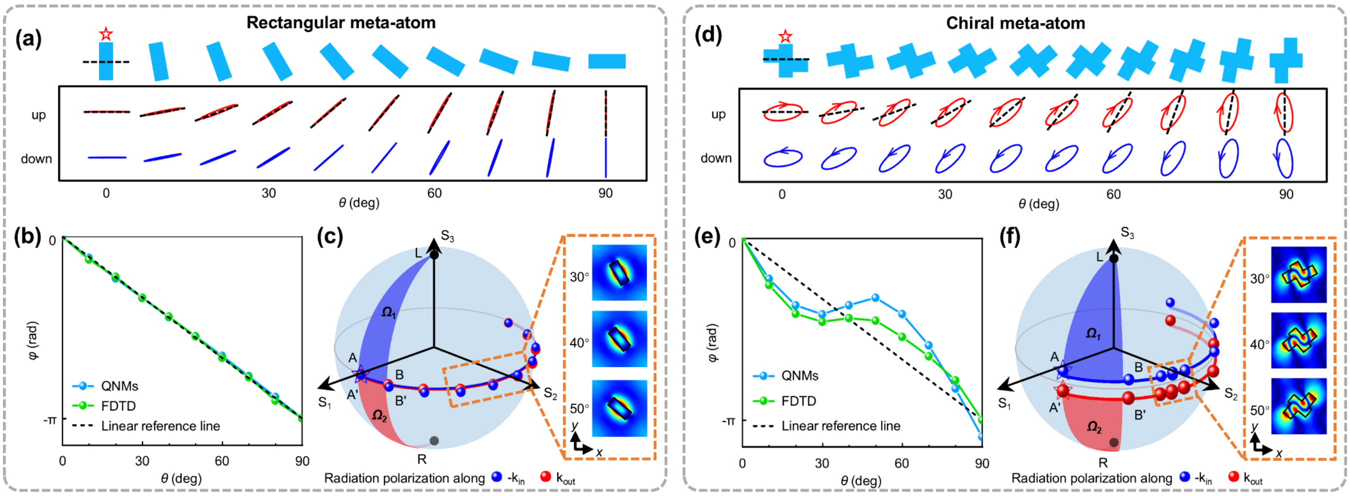

Figure 2. (a, d) Schematics of far-field radiation polarization states of meta-atoms as the orientation angle varies from 0° to 90° in 10° increments. Here the ellipticity was slightly increased for better visualization. Red: upward radiation (k_{out}, i.e., k_0). Blue: downward radiation ($-k_{in}$, i.e., $-k_0$). The dashed line indicates the orientation of the structure. (b, e) The geometric phase calculated through the QNMs method (blue dot-dashed line) and FDTD simulation (green dot-dashed line). The 2-fold linear reference is shown as the black dashed line. (c, f) Far-field radiation polarization on the Poincaré sphere under LCP incidence, L (R) represent the polarization state of the incident (projected) light. Red and blue spheres represent the polarization states of mode radiations along the radiation direction (k_{out}) and opposite to the incident direction ($-k_{in}$), respectively. The red (blue) area is related to the geometric phase by $\varphi_2 = {}^1/_2\Omega_2$ ($\varphi_1 = {}^1/_2\Omega_1$), where Ω_2 and Ω_1 are the solid angle of the corresponding geodesic triangle. The right panel shows part of the electric field distribution.

effect between neighboring atoms [the difference would gradually disappear with larger P; see the blue lines P = 1800 nm in Figure 1(b, c, e, f)]. The light field in adjacent chiral structures couples to each other due to field overlap, as evidenced by the different field distributions under different boundary conditions in simulations (see section S2 in the Supporting Information). The coupling strength dependents on the relative position of neighboring structures, which vary with the rotation of meta-atoms. This rotation-dependent coupling of the chiral atoms gives rise to the linear-oscillated geometric phase. The following results focus on a period of 1500 nm. Similar results for the period of 900 nm are provided in section S9 in the Supporting Information.

Next, to conduct the quantitative analysis of the coupling induced linear-to-oscillatory phase behavior, we introduced the QNM technique.[44] Here, we consider the system of two meta-atoms with different orientation angles. The optical response of an open system can be interpreted through QNMs expansion, and based on the reciprocity, the scattered field along the projected polarization (i.e., analyzed by RCP component) can be expressed as (details are provided in section S3 in the Supporting Information):

$$\mathbf{E}_{\mathrm{sca}}^{R} \propto \mathbf{J}_{\mathrm{R}}\left[\cos\left(\frac{1}{2}\widehat{\mathrm{LA}}\right)\cos\left(\frac{1}{2}\widehat{\mathrm{A'R}}\right)E_{\mathrm{A}} + \cos\left(\frac{1}{2}\widehat{\mathrm{LB}}\right)\cos\left(\frac{1}{2}\widehat{\mathrm{B'R}}\right)E_{\mathrm{B}}\exp[i(\varphi_1+\varphi_2)]\right] \quad (1)$$

where $\mathbf{J}_{\mathrm{R}}$ is the Jones vector of RCP (termed as R), L represents the incident polarization (LCP) mapping on the Poincaré sphere, A and B are the two QNM radiation polarizations of the two rotated meta-atoms in the opposite incident direction (i.e., $-k_{in}$), A′ and B′ are the radiation polarizations along the transmission direction (i.e., k_{out}), $\widehat{LA}$($\widehat{LB}$, $\widehat{A'R}$, $\widehat{B'R}$)corresponds to the length of the great arc connecting LA(LB, A′R, B′R) on the Poincaré sphere. $\varphi_{1+}\varphi_2$ is the total geometric phase. The first term φ_1 is a geometric phase induced by the excitation process (the incident LCP wave excites the two QNMs, respectively), which is half of the solid angle of the geodesic triangle of LAB on the Poincaré sphere [see Figure 2(c, f), $\varphi_1 = {}^1/_2\Omega_1$]. The second geometric phase term φ_2 is induced by the polarization projection process (the radiated fields of the two QNMs are projected to the targeted polarization of interest, e.g. RCP in our study), which is half of the solid angle of the geodesic triangle of A′RB′ on the Poincaré sphere [see Figure 2(c, f), $\varphi_2 = {}^1/_2\Omega_2$].

In periodic structures, the polarization vector $\vec{c}$ of far-field radiation in reciprocal space can be computed by the following Fourier transform:[50]

$$\vec{c}_{\uparrow,\downarrow}(k_x, k_y) = (c_{x\_\uparrow,\downarrow}, c_{y\_\uparrow,\downarrow}) = \iint_{\mathrm{cell}_{\uparrow,\downarrow}} \mathrm{e}^{ik_x x + ik_y y}(E_x^{k_x,k_y}(x, y), E_y^{k_x,k_y}(x, y))\mathrm{d}x\,\mathrm{d}y \Big/ \iint_{\mathrm{cell}_{\uparrow,\downarrow}} \mathrm{d}x\,\mathrm{d}y \quad (2)$$

where the up and down arrows (↑, ↓) respectively indicate the upward (along the transmission direction, k_{out}) and downward (opposite to the incident direction, $-k_{in}$) direction along the $\pm z$ axis, and the term $\mathrm{cell}_{\uparrow,\downarrow}$ refers to the integration surface

https://doi.org/10.1021/acs.nanolett.6c02125
Nano Lett. XXXX, XXX, XXX−XXX

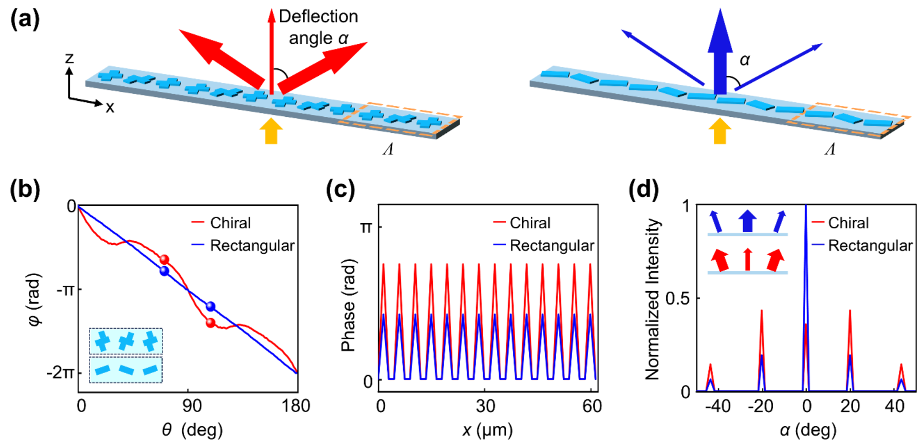

Figure 3. (a) Schematic illustration of beam deflection. (b) PB phase of chiral and rectangular meta-atoms. Red and blue markers indicate the phase values corresponding to orientation angles (71° and 109°). The inset provides a visualization of one unit cell for the chiral (top) and rectangular (bottom) structures. (c) Phase profiles of metasurfaces composed of chiral (red) and rectangular (blue) meta-atoms. (d) Theoretically calculated far-field radiation patterns for chiral and rectangular metasurfaces.

above and below the meta-atom in one unit cell. k_x and k_y are the Bloch momentum in the x- and y-direction, and E_x and E_y are the electrical field components. Since we only focus on the PB phase response of normal incident and transmitted light, the Bloch vectors k_x and k_y are chosen as $k_x = k_y = 0$, and only E_x and E_y components of the QNMs field are considered. The integration is performed over one unit cell. Each polarization state can be located on the Poincaré sphere with Stokes parameters S_0, S_1, S_2, and S_3 ($S_0 = |c_x|^2 + |c_y|^2$, $S_1 = |c_x|^2 - |c_y|^2$, $S_2 = 2\mathrm{Re}(c_x c^*_y)$, $S_3 = -2\mathrm{Im}(c_x c^*_y)$). For QNM analysis, to capture the essential physical principles, we neglect the substrate (to exclude the extra-essential or even fictitious modes) and thus both types of meta-atoms are mirror-symmetric with respect to the $x-y$ plane. We calculate the upward and downward far-field polarization states ($k_x = k_y = 0$, $k_z = \pm k_0$) of QNMs for rectangular and chiral meta-atoms as a function of orientation angle from 0° to 90° (see Figure 2(a, d) for schematics and details in section S4 in the Supporting Information). The mirror symmetry along the z-axis of the structures guarantee that the polarizations along the upward and downward directions have the same S_{12} and opposite S_3, i.e., $S_{1,2}\_\uparrow = S_{1,2}\_\downarrow$ and $S_3\_\uparrow = -S_3\_\downarrow$. The red line indicates the far-field polarization of upward radiation (k_{out}, i.e., k_0), and the blue line represents that of downward radiation ($-k_{in}$, i.e., $-k_0$). By mapping the polarization states on the Poincaré sphere, we can visualize the far-field polarization state trajectory with respect to different atom orientations, as depicted in Figure 2(c, f). The far-field polarizations at every 10° orientation angles are represented by red and blue sphere markers (they are connected by great-circle arcs).

In the case of rectangular meta-atom, the near-field distributions of adjacent meta-atoms remain largely independent because of weak coupling effects, and the electric field distribution (electric dipole mode) rigidly rotates in precise alignment with the structural orientation [see the right panel of Figure 2(c) consisting the electric fields within θ = 30°−50° for example, more results are shown in Figure S3a]. Therefore, the radiation polarization state of their QNMs also rotates rigidly with the structural orientation angle θ [Figure 2(a), the black dotted line corresponds to the structure orientation], and due to the electric dipole mode characteristics, the radiation polarization states opposite to the incident direction (downward) and along the transmission direction (upward) are the same with each other, namely, A = A′, and B = B′. As a result, the trajectory of the polarization state lies uniformly near the equator of the Poincaré sphere, as shown in Figure 2(c), leading to a linear relationship between the PB phase φ and θ, which constitutes the physical origin of the conventional geometric phase.

In contrast, for the presented chiral meta-atoms, their rotation introduces significant near-field coupling between neighboring structures, and their electric field distribution distorts nonuniformly. For example, even though the chiral structure rotates from θ = 30° to 50°, the electric field distribution does not change significantly [see the right panel in Figure 2(f)]. More results for θ = 0° ≈ 90° are provided in Figure S3b. These variations subsequently alter the radiation polarization of the QNMs [Figure 2(d)], causing the polarization trajectory to distribute nonuniformly on the Poincaré sphere and giving rise to the linear-oscillated phase response.

The calculated geometric phase φ under our QNMs framework is shown in Figure 2(b, e) as blue dot-dashed line. They are generally consistent with the results of FDTD simulations (green dot-dashed line) for both chiral and rectangular structures. The slight difference between QNMs and FDTD results [Figure 2(e)] is due to the substrate difference, where we consider the substrate in FDTD simulation while excluding it in QNMs analysis. The black dashed line is the ideal linear case with $\varphi = -2\theta$ (it would be $\varphi = 2\theta$ for the RCP incidence). For the rectangular structure (Figure 2(b), both the FDTD simulated phase and the QNM calculated phase all closely follow the ideal linear line, indicating that the conventional geometric phase evolution is primarily dictated by the structure's orientation, with minimal influence from additional structural coupling effects. In contrast, for the chiral structure (Figure 2(e)), the geometric phase exhibits oscillations that deviates from the linear dependence ($\varphi = -2\theta + \delta$), in which the oscillated term δ coming from the non-negligible coupling effects. Although we utilize chiral meta-atoms to demonstrate the strong coupling regime here, we emphasize that the physical mechanism is universally driven by the near-field interaction regardless of the geometric chirality (see detailed analysis in sections S11 and

https://doi.org/10.1021/acs.nanolett.6c02125
Nano Lett. XXXX, XXX, XXX−XXX

S15 in the Supporting Information). In addition, the Quantitative measurements of near-field coupling strengths via transmission mode-splitting theory are provided in section S16 in the Supporting Information.

After clarifying the origin of the generalized geometric phase (i.e., far-field polarization rotations) in metasurfaces both for weak coupling case (e.g., the presented rectangular atom) and strong coupling case (e.g., the presented chiral atom) based on the QNM framework, we then design metasurfaces for beam deflection based on these meta-atoms with identical structure orientation angles to characterize the different geometric phase responses. Since the two kinds of meta-atoms exhibit different dependence of the PB phase on the structural orientation, these two metasurfaces would show different beam deflection abilities in beam deflection directions and intensities, as shown in Figure 3(a). Structural orientation angles are optimized (supposing they have the same transmittances) by particle-swarm-optimization algorithm to maximize the contrast in beam deflection performance between the two metasurfaces. The center-to-center distance between adjacent meta-atoms is set to 1500 nm, and a cyclical arrangement of three meta-atoms with orientation angles of 109°, 71°, and 109° is implemented with the period of one unit cell $\Lambda = 4.5$ μm. These orientation angles and their corresponding PB phases are illustrated in Figure 3(b), and the phase profiles $\varphi(x)$ of the two metasurfaces are depicted in Figure 3(c). The far-field radiation patterns are computed based on the Fourier transform of the near field in simulation, with corresponding results presented in Figure 3(d). It can be observed that the energy of the chiral metasurface is mainly concentrated around $\alpha = \pm 20°$, while that of the rectangular metasurface is primarily concentrated at $\alpha = 0°$. Such deflection difference of intensity distribution is totally attributed to the different PB phase response, since we only consider the phase and assuming the uniform transmittances in the theoretical calculation. For further verification, we added the specific transmission of the selected rectangular and chiral structures, and calculated the far-field radiation (see Supporting Information S5), which is basically similar to that in Figure 3(d), indicating the predominant effect of phase response.

To further verify the different beam deflection abilities between the two metasurfaces, we perform numerical simulations and experimental characterizations. In the FDTD simulation, a single row of the structure with periodic boundary conditions along the y-axis is used to reduce the computational cost, and the corresponding simulated normalized far-field intensity distributions $|E|^2$ are presented in Figure 4(a) for the rectangular structure and Figure 4(d) for the chiral structure. The transmitted light predominantly remains at 0° after passing through the rectangular meta-atoms, while it is deflected to $\alpha = \pm 20°$ by the chiral structures. In the experiment, we fabricated the metasurfaces based on the electron-beam lithography (see section S6 in the Supporting Information for details) and the corresponding scanning electron microscope (SEM) images of the samples are shown in Figure 4(b, e). In the experimental setup, the incident light is generated by a white light supercontinuum laser (Fianium Supercontinuum, 4 W). After being filtered and polarized, the LCP light at $\lambda = 1550$ nm is incident to the sample. The transmitted signal is collected by an objective and then is Fourier-transformed by a lens. More details of the experimental setup are provided in section S7 in the Supporting Information. The CCD captured results are shown in Figure 4(c, f). For the rectangular meta-atom sample (Figure 4(c)), the transmitted light mainly remains at 0°, while it is deflected to ±20° by the chiral structures (Figure 4(f)). Since we have incorporated a circular polarizer in the transmission path to filter the interested RCP components, the symmetric pattern emerges rather than the usual one-sided pattern is due to the periodic phase profile, which differs from the typical continuous phase profile used in standard meta-deflectors. The theoretical calculation, FDTD simulation and experimental results are approximately in good consistency (see section S8 in the Supporting Information). And the analysis of the operational wavelength bandwidth of the proposed effect and device performance are provided in section S12 in the Supporting Information.

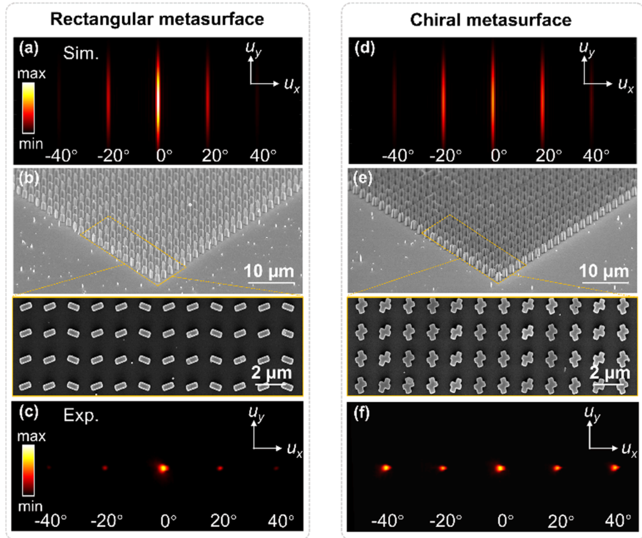

Figure 4. (a, d) FDTD-simulated far-field radiation patterns of metasurfaces. (b, e) Scanning electron microscopy (SEM) images of the fabricated metasurfaces. The fabricated samples have dimensions of 400 μm × 400 μm. (c, f) Experimentally measured far-field radiation patterns of metasurfaces.

Furthermore, metasurfaces with $P = 900$ nm were also designed and experimentally characterized. The metasurfaces based on rectangular and chiral meta-atoms with the same structure orientations show distinct beam deflection abilities as well (see section S9 in the Supporting Information). Our results indicate that the coupling effects and resulting PB phase response deviation are not unique exceptions in complex nanostructures.

In addition to the example of beam deflection metasurfaces, we have also provided a specific example of optimizing a high-NA metamaterial lens using the QNM framework, which is provided in section S14 in the Supporting Information.

It is worth noting that, in recent years, the effects of nonlocality in metasurfaces have been extensively studied,[51−54] with particular emphasis on the crucial role of coupling between meta-atoms. To model these nonlocal systems, spatiotemporal coupled mode theory (STCMT) has been developed in previous works.[54] However, our quasi-normal-mode (QNM) methods provide distinctive features that are not available in traditional STCMT. For example, the QNM framework is inherently vectorial and explicitly incorporates the incident polarization, allowing polarization-dependent responses to be rigorously explained rather than simply described (see section S10 in the Supporting Information).

https://doi.org/10.1021/acs.nanolett.6c02125
Nano Lett. XXXX, XXX, XXX−XXX

In this context, QNM methods present a novel approach for investigating the rapidly advancing field of nonlocal metasurfaces.

In summary, this study highlights a profound difference in the geometric phase response of coupled meta-atoms, underscoring a deeper and broader physical mechanism often overlooked in previous research, where the geometric phase is reduced to its simplest form. In contrast to the linear phase-orientation relationship observed in rectangular meta-atoms (this aligns with conventional geometric phase principles), the geometric phase response of chiral meta-atoms exhibits a more sophisticated dependence on the atom orientation angle induced by intricate coupling among chiral meta-atoms. To explain this behavior in such coupled structures, QNM theory is employed. The geometric phase extracted from far-field radiation polarizations of QNMs demonstrates good agreement with the geometric phase obtained from FDTD simulations, indicating that this theory provides an accurate description of the generalized geometric phase beyond the linear dependence regime. Furthermore, the different geometric phase responses of chiral and rectangular meta-atoms are theoretically and experimentally validated by designing beam-steering metasurfaces. The different beam deflection capabilities of the two metasurfaces with identical structure orientation angles arise directly from the distinct PB phase responses, which is consistent with our theoretical analysis. This research not only deepens the fundamental interpretation of geometric phase in complex coupled meta-atoms but also contributes to the conceptual understanding required for advanced optical devices with sophisticated wavefront manipulation capabilities and offers new perspectives for related disciplines of integrated photonics, biosensing, and imaging.

■ ASSOCIATED CONTENT

Supporting Information

The Supporting Information is available free of charge at https://pubs.acs.org/doi/10.1021/acs.nanolett.6c02125.

> Detailed PB phase calculation procedures supported by finite-difference time-domain (FDTD) simulations; Electric field modes with coupling (Periodic Boundary Condition, PBC) and without coupling (Perfectly Matched Layers, PML); QNM analysis; Electric mode distributions of meta-atoms with structure rotation; More details of far-field radiation patterns; Fabrication section; Optical setup for characterizing the metasurfaces with beam deflection functionality; Comparison between experimental, simulated and theoretical results for metasurfaces with P = 1500 nm; Design and performance analysis of metasurfaces with P = 900 nm; Comparison between spatiotemporal coupled mode theory (STCMT) and quasi-normal mode (QNM) approach; Dependence of geometric phase deviations on structural symmetries and near-field spatial overlaps; Broadband wavelength dependence of geometric phase response and far-field scattering distributions; Morphological characterization of fabricated samples and tolerance analysis against structural tilting; Analysis and coupling-corrected phase optimization for high-numerical-aperture (high-NA) metalenses; Geometric phase variations under different periods of different structural complexities; Quantitative measurement of near-field coupling strengths via transmission mode-splitting characteristics (PDF)

■ AUTHOR INFORMATION

Corresponding Authors

Chen Chen − *National Laboratory of Solid State Microstructures, Key Laboratory of Intelligent Optical Sensing and Manipulation, Jiangsu Key Laboratory of Artificial Functional Materials, College of Engineering and Applied Sciences, Nanjing University, Nanjing 210093, China*; Email: chenchen2021@nju.edu.cn

Wei Liu − *College for Advanced Interdisciplinary Studies and Nanhu Laser Laboratory and Hunan Provincial Key Laboratory of Novel Nano-Optoelectronic Information Materials and Devices, National University of Defense Technology, Changsha 410073, People's Republic of China*; orcid.org/0000-0002-7067-6239; Email: wei.liu.pku@gmail.com

Tao Li − *National Laboratory of Solid State Microstructures, Key Laboratory of Intelligent Optical Sensing and Manipulation, Jiangsu Key Laboratory of Artificial Functional Materials, College of Engineering and Applied Sciences, Nanjing University, Nanjing 210093, China*; orcid.org/0000-0003-0049-471X; Email: taoli@nju.edu.cn

Authors

Yue Wang − *National Laboratory of Solid State Microstructures, Key Laboratory of Intelligent Optical Sensing and Manipulation, Jiangsu Key Laboratory of Artificial Functional Materials, College of Engineering and Applied Sciences, Nanjing University, Nanjing 210093, China*

Shengjie Wu − *National Laboratory of Solid State Microstructures, Key Laboratory of Intelligent Optical Sensing and Manipulation, Jiangsu Key Laboratory of Artificial Functional Materials, College of Engineering and Applied Sciences, Nanjing University, Nanjing 210093, China*

Xiaomin Du − *National Laboratory of Solid State Microstructures, Key Laboratory of Intelligent Optical Sensing and Manipulation, Jiangsu Key Laboratory of Artificial Functional Materials, College of Engineering and Applied Sciences, Nanjing University, Nanjing 210093, China*

Jitao Ji − *National Laboratory of Solid State Microstructures, Key Laboratory of Intelligent Optical Sensing and Manipulation, Jiangsu Key Laboratory of Artificial Functional Materials, College of Engineering and Applied Sciences, Nanjing University, Nanjing 210093, China*

Jian Li − *National Laboratory of Solid State Microstructures, Key Laboratory of Intelligent Optical Sensing and Manipulation, Jiangsu Key Laboratory of Artificial Functional Materials, College of Engineering and Applied Sciences, Nanjing University, Nanjing 210093, China*

Jiacheng Sun − *National Laboratory of Solid State Microstructures, Key Laboratory of Intelligent Optical Sensing and Manipulation, Jiangsu Key Laboratory of Artificial Functional Materials, College of Engineering and Applied Sciences, Nanjing University, Nanjing 210093, China*

Xueyun Li − *National Laboratory of Solid State Microstructures, Key Laboratory of Intelligent Optical Sensing and Manipulation, Jiangsu Key Laboratory of Artificial Functional Materials, College of Engineering and Applied Sciences, Nanjing University, Nanjing 210093, China*

https://doi.org/10.1021/acs.nanolett.6c02125
Nano Lett. XXXX, XXX, XXX−XXX

Wange Song — *National Laboratory of Solid State Microstructures, Key Laboratory of Intelligent Optical Sensing and Manipulation, Jiangsu Key Laboratory of Artificial Functional Materials, College of Engineering and Applied Sciences, Nanjing University, Nanjing 210093, China*

Shining Zhu — *National Laboratory of Solid State Microstructures, Key Laboratory of Intelligent Optical Sensing and Manipulation, Jiangsu Key Laboratory of Artificial Functional Materials, College of Engineering and Applied Sciences, Nanjing University, Nanjing 210093, China*

Complete contact information is available at: https://pubs.acs.org/10.1021/acs.nanolett.6c02125

Author Contributions

[∇]Authors Y. Wang, S. Wu, C. Chen, and X. Du contributed equally to this work. C.C., W.L., and T.L. designed and supervised the study. Y.W., S.W., and X.D. carried out simulations and performed data analysis. J.L. and J.S. fabricated the experimental samples, Y.W. carried out experimental measurements with the help of J.J. and X.L. C.C., W.S., W.L., and T.L. conducted data interpretation and manuscript writing. C.C., W.L., S.Z., and T.L. provided financial support.

Notes

The authors declare no competing financial interest.

■ ACKNOWLEDGMENTS

The authors acknowledge the microfabrication center of the National Laboratory of Solid State Microstructures (NLSSM) for technical support. The authors acknowledge the funding provided by National Key Research and Development Program of China (2024YFA1012600, 2022YFA1404301), National Natural Science Foundation of China (Nos. 62325504, 62305149, 92250304, 62288101), Outstanding Young Researcher scheme of Hunan Province No. 2024JJ2056, and Dengfeng Project B of Nanjing University.

■ REFERENCES

(1) Kildishev, A. V.; Boltasseva, A.; Shalaev, V. M. Planar Photonics with Metasurfaces. *Science* **2013**, *339* (6125), No. 1232009.

(2) Yu, N.; Genevet, P.; Kats, M. A.; Aieta, F.; Tetienne, J.-P.; Capasso, F.; Gaburro, Z. Light Propagation with Phase Discontinuities: Generalized Laws of Reflection and Refraction. *Science* **2011**, *334* (6054), 333−337.

(3) Lin, D.; Fan, P.; Hasman, E.; Brongersma, M. L. Dielectric gradient metasurface optical elements. *Science* **2014**, *345* (6194), 298−302.

(4) Li, Z.; Palacios, E.; Butun, S.; Aydin, K. Visible-Frequency Metasurfaces for Broadband Anomalous Reflection and High-Efficiency Spectrum Splitting. *Nano Lett.* **2015**, *15* (3), 1615−1621.

(5) Chen, C.; Ye, X.; Sun, J.; Chen, Y.; Huang, C.; Xiao, X.; Song, W.; Zhu, S.; Li, T. Bifacial-metasurface-enabled pancake metalens with polarized space folding. *Optica* **2022**, *9* (12), 1314−1322.

(6) Khorasaninejad, M.; Chen, W. T.; Devlin, R. C.; Oh, J.; Zhu, A. Y.; Capasso, F. Metalenses at visible wavelengths: Diffraction-limited focusing and subwavelength resolution imaging. *Science* **2016**, *352* (6290), 1190−1194.

(7) Wang, Y.; Chen, C.; Wu, S.; Ye, X.; Zhu, S.; Li, T. Metalens with tilted structures for high-efficiency focusing at large-angle incidences. *Chin. Opt. Lett.* **2024**, *22* (5), No. 053601.

(8) Ye, X.; Qian, X.; Chen, Y.; Yuan, R.; Xiao, X.; Chen, C.; Hu, W.; Huang, C.; Zhu, S.; Li, T. Chip-scale metalens microscope for wide-field and depth-of-field imaging. *Adv. Photonics* **2022**, *4* (4), No. 046006.

(9) Zou, X.; Zheng, G.; Yuan, Q.; Zang, W.; Chen, R.; Li, T.; Li, L.; Wang, S.; Wang, Z.; Zhu, S. Imaging based on metalenses. *PhotoniX* **2020**, *1* (1), 2.

(10) Chen, W. T.; Yang, K.-Y.; Wang, C.-M.; Huang, Y.-W.; Sun, G.; Chiang, I. D.; Liao, C. Y.; Hsu, W.-L.; Lin, H. T.; Sun, S.; et al. High-Efficiency Broadband Meta-Hologram with Polarization-Controlled Dual Images. *Nano Lett.* **2014**, *14* (1), 225−230.

(11) Huang, L.; Zhang, S.; Zentgraf, T. Metasurface holography: from fundamentals to applications. *Nanophotonics* **2018**, *7* (6), 1169−1190.

(12) Feng, C.; He, T.; Shi, Y.; Song, Q.; Zhu, J.; Zhang, J.; Wang, Z.; Tsai, D. P.; Cheng, X. Diatomic Metasurface for Efficient Six-Channel Modulation of Jones Matrix. *Laser Photonics Rev.* **2023**, *17* (8), No. 2200955.

(13) Huang, Y.-W.; Chen, W. T.; Tsai, W.-Y.; Wu, P. C.; Wang, C.-M.; Sun, G.; Tsai, D. P. Aluminum Plasmonic Multicolor Meta-Hologram. *Nano Lett.* **2015**, *15* (5), 3122−3127.

(14) Wang, L.; Kruk, S.; Tang, H.; Li, T.; Kravchenko, I.; Neshev, D. N.; Kivshar, Y. S. Grayscale transparent metasurface holograms. *Optica* **2016**, *3* (12), 1504−1505.

(15) Ni, X.; Kildishev, A. V.; Shalaev, V. M. Metasurface holograms for visible light. *Nat. Commun.* **2013**, *4* (1), 2807.

(16) Chen, C.; Xiao, X.; Ye, X.; Sun, J.; Ji, J.; Yu, R.; Song, W.; Zhu, S.; Li, T. Neural network assisted high-spatial-resolution polarimetry with non-interleaved chiral metasurfaces. *Light Sci. Appl.* **2023**, *12* (1), 288.

(17) Divitt, S.; Zhu, W.; Zhang, C.; Lezec, H. J.; Agrawal, A. Ultrafast optical pulse shaping using dielectric metasurfaces. *Science* **2019**, *364* (6443), 890−894.

(18) Li, G.; Kang, M.; Chen, S.; Zhang, S.; Pun, E. Y.-B.; Cheah, K. W.; Li, J. Spin-Enabled Plasmonic Metasurfaces for Manipulating Orbital Angular Momentum of Light. *Nano Lett.* **2013**, *13* (9), 4148−4151.

(19) Liu, H.; Mehmood, M. Q.; Huang, K.; Ke, L.; Ye, H.; Genevet, P.; Zhang, M.; Danner, A.; Yeo, S. P.; Qiu, C.-W.; Teng, J. Twisted Focusing of Optical Vortices with Broadband Flat Spiral Zone Plates. *Adv. Opt. Mater.* **2014**, *2* (12), 1193−1198.

(20) Yu, N.; Aieta, F.; Genevet, P.; Kats, M. A.; Gaburro, Z.; Capasso, F. A. Broadband, Background-Free Quarter-Wave Plate Based on Plasmonic Metasurfaces. *Nano Lett.* **2012**, *12* (12), 6328−6333.

(21) Sun, S.; He, Q.; Xiao, S.; Xu, Q.; Li, X.; Zhou, L. Gradient-index meta-surfaces as a bridge linking propagating waves and surface waves. *Nat. Mater.* **2012**, *11* (5), 426−431.

(22) Sun, S.; Yang, K.-Y.; Wang, C.-M.; Juan, T.-K.; Chen, W. T.; Liao, C. Y.; He, Q.; Xiao, S.; Kung, W.-T.; Guo, G.-Y.; Zhou, L.; Tsai, D. P. High-Efficiency Broadband Anomalous Reflection by Gradient Meta-Surfaces. *Nano Lett.* **2012**, *12* (12), 6223−6229.

(23) Arbabi, A.; Horie, Y.; Ball, A. J.; Bagheri, M.; Faraon, A. Subwavelength-thick lenses with high numerical apertures and large efficiency based on high-contrast transmitarrays. *Nat. Commun.* **2015**, *6* (1), 7069.

(24) Fan, Z.-B.; Shao, Z.-K.; Xie, M.-Y.; Pang, X.-N.; Ruan, W.-S.; Zhao, F.-L.; Chen, Y.-J.; Yu, S.-Y.; Dong, J.-W. Silicon Nitride Metalenses for Close-to-One Numerical Aperture and Wide-Angle Visible Imaging. *Phys. Rev. Appl.* **2018**, *10* (1), No. 014005.

(25) Khorasaninejad, M.; Zhu, A. Y.; Roques-Carmes, C.; Chen, W. T.; Oh, J.; Mishra, I.; Devlin, R. C.; Capasso, F. Polarization-Insensitive Metalenses at Visible Wavelengths. *Nano Lett.* **2016**, *16* (11), 7229−7234.

(26) Berry, M. V. The Adiabatic Phase and Pancharatnam's Phase for Polarized Light. *J. Mod. Opt.* **1987**, *34* (11), 1401−1407.

(27) Bomzon, Z. e.; Biener, G.; Kleiner, V.; Hasman, E. Space-variant Pancharatnam-Berry phase optical elements with computer-generated subwavelength gratings. *Opt. Lett.* **2002**, *27* (13), 1141−1143.

(28) Cohen, E.; Larocque, H.; Bouchard, F.; Nejadsattari, F.; Gefen, Y.; Karimi, E. Geometric phase from Aharonov-Bohm to Pancharatnam-Berry and beyond. *Nat. Rev. Phys.* **2019**, *1* (7), 437−449.

(29) Jisha, C. P.; Nolte, S.; Alberucci, A. Geometric Phase in Optics: From Wavefront Manipulation to Waveguiding. *Laser Photonics Rev.* **2021**, *15* (10), No. 2100003.
(30) Wen, D.; Yue, F.; Liu, W.; Chen, S.; Chen, X. Geometric Metasurfaces for Ultrathin Optical Devices. *Adv. Opt. Mater.* **2018**, *6* (17), No. 1800348.
(31) Guo, Y.; Pu, M.; Zhang, F.; Xu, M.; Li, X.; Ma, X.; Luo, X. Classical and generalized geometric phase in electromagnetic metasurfaces. *Photonics Insights* **2022**, *1* (1), R03.
(32) Chen, Y.; Jiang, M.; Zhang, F.; Pu, M.; Chen, L.; Guo, Y.; Xu, M.; He, Q.; Gao, P.; Ma, X.; Luo, X. Global Selection Rules and Giant Enhanced Harmonic Generations in LiNbO3 Nonlinear Meta-Optics. *Laser Photonics Rev.* **2025**, *19* (4), No. 2400991.
(33) Huang, L.; Chen, X.; Mühlenbernd, H.; Li, G.; Bai, B.; Tan, Q.; Jin, G.; Zentgraf, T.; Zhang, S. Dispersionless Phase Discontinuities for Controlling Light Propagation. *Nano Lett.* **2012**, *12* (11), 5750−5755.
(34) He, C.; Sun, T.; Guo, J.; Cao, M.; Xia, J.; Hu, J.; Yan, Y.; Wang, C. Chiral Metalens of Circular Polarization Dichroism with Helical Surface Arrays in Mid-Infrared Region. *Adv. Opt. Mater.* **2019**, *7* (24), No. 1901129.
(35) Karakasoglu, I.; Xiao, M.; Fan, S. Polarization control with dielectric helix metasurfaces and arrays. *Opt. Express* **2018**, *26* (17), 21664−21674.
(36) Chen, C.; Gao, S.; Song, W.; Li, H.; Zhu, S.-N.; Li, T. Metasurfaces with Planar Chiral Meta-Atoms for Spin Light Manipulation. *Nano Lett.* **2021**, *21* (4), 1815−1821.
(37) Deng, Q.; Yang, J.; Lan, X.; Zhang, W.; Cui, H.; Xie, Z.; Li, L.; Huang, Y. Investigations of generalized Pancharatnam-Berry phase in all-dielectric metasurfaces. *Results Phys.* **2023**, *51*, No. 106730.
(38) Xie, X.; Pu, M.; Jin, J.; Xu, M.; Guo, Y.; Li, X.; Gao, P.; Ma, X.; Luo, X. Generalized Pancharatnam-Berry Phase in Rotationally Symmetric Meta-Atoms. *Phys. Rev. Lett.* **2021**, *126* (18), No. 183902.
(39) Naeem, T.; Kim, J.; Khaliq, H. S.; Seong, J.; Chani, M. T. S.; Tauqeer, T.; Mehmood, M. Q.; Massoud, Y.; Rho, J. Dynamic Chiral Metasurfaces for Broadband Phase-Gradient Holographic Displays. *Adv. Opt. Mater.* **2023**, *11* (5), No. 2202278.
(40) Mun, J.; Kim, M.; Yang, Y.; Badloe, T.; Ni, J.; Chen, Y.; Qiu, C.-W.; Rho, J. Electromagnetic chirality: from fundamentals to nontraditional chiroptical phenomena. *Light Sci. Appl.* **2020**, *9* (1), 139.
(41) Jeon, D.; Kim, H.; Rho, J. Leaky Guided Mode-Induced Large-Angle Nonlocal Metasurfaces. *ACS Photonics* **2025**, *12* (1), 375−383.
(42) Bai, Q.; Perrin, M.; Sauvan, C.; Hugonin, J. P.; Lalanne, P. Efficient and intuitive method for the analysis of light scattering by a resonant nanostructure. *Opt. Express* **2013**, *21* (22), 27371−27382.
(43) Huang, L.; Xu, L.; Powell, D. A.; Padilla, W. J.; Miroshnichenko, A. E. Resonant leaky modes in all-dielectric metasystems: Fundamentals and applications. *Phys. Rep.* **2023**, *1008*, 1−66.
(44) Kristensen, P. T.; de Lasson, J. R.; Gregersen, N. Calculation, normalization, and perturbation of quasinormal modes in coupled cavity-waveguide systems. *Opt. Lett.* **2014**, *39* (22), 6359−6362.
(45) Kristensen, P. T.; de Lasson, J. R.; Heuck, M.; Gregersen, N.; Mørk, J. On the Theory of Coupled Modes in Optical Cavity-Waveguide Structures. *J. Lightwave Technol.* **2017**, *35* (19), 4247−4259.
(46) Lalanne, P.; Yan, W.; Vynck, K.; Sauvan, C.; Hugonin, J.-P. Light Interaction with Photonic and Plasmonic Resonances. *Laser Photonics Rev.* **2018**, *12* (5), No. 1700113.
(47) Wu, T.; Gurioli, M.; Lalanne, P. Nanoscale Light Confinement: the Q's and V's. *ACS Photonics* **2021**, *8* (6), 1522−1538.
(48) Yan, W.; Faggiani, R.; Lalanne, P. Rigorous modal analysis of plasmonic nanoresonators. *Phys. Rev. B* **2018**, *97* (20), No. 205422.
(49) Wang, P.; Chen, Y.; Liu, W. Geometric Phase-Driven Scattering Evolutions. *Phys. Rev. Lett.* **2024**, *133* (9), No. 093801.
(50) Kang, M.; Mao, L.; Zhang, S.; Xiao, M.; Xu, H.; Chan, C. T. Merging bound states in the continuum by harnessing higher-order topological charges. *Light Sci. Appl.* **2022**, *11* (1), 228.
(51) Overvig, A. C.; Malek, S. C.; Yu, N. Multifunctional Nonlocal Metasurfaces. *Phys. Rev. Lett.* **2020**, *125* (1), No. 017402.
(52) Overvig, A.; Alù, A. Diffractive Nonlocal Metasurfaces. *Laser Photonics Rev.* **2022**, *16* (8), No. 2100633.
(53) Shastri, K.; Monticone, F. Nonlocal flat optics. *Nat. Photonics* **2023**, *17* (1), 36−47.
(54) Overvig, A.; Mann, S. A.; Alù, A. Spatio-temporal coupled mode theory for nonlocal metasurfaces. *Light Sci. Appl.* **2024**, *13* (1), 28.

https://doi.org/10.1021/acs.nanolett.6c02125
Nano Lett. XXXX, XXX, XXX−XXX